Quantitative description of charge-carrier transport in a white organic light-emitting diode

M. Schober,* M. Anderson, M. Thomschke, J. Widmer, M. Furno, R. Scholz, B. Lüssem, and K. Leo
Institut für Angewandte Photophysik, Technische Universität Dresden, DE-01062 Dresden, Germany
(Received 18 July 2011; published 24 October 2011)

We present a simulation model for the analysis of charge-carrier transport in organic thin-film devices, and apply it to a three-color white hybrid organic light-emitting diode (OLED) with fluorescent blue and phosphorescent red and green emission. We simulate a series of single-carrier devices, which reconstruct the OLED layer sequence step by step. Thereby, we determine the energy profiles for hole and electron transport, show how to discern bulk from interface limitation, and identify trap states.

DOI: 10.1103/PhysRevB.84.165326 PACS number(s): 81.05.Fb

I. INTRODUCTION

State-of-the-art organic light-emitting diodes (OLEDs) for lighting and display applications use sophisticated organic multilayer structures.[1–10] Their development and optimization require a fundamental understanding of the optical and electrical device properties. Over the past years, the investigations on charge-carrier transport in organic semiconductor materials showed a variety of different mechanisms, which mainly result from different morphologies and different degrees of crystallinity. Consequently, the developed transport models often envisage different situations from purely disordered[11,12] to highly ordered systems.[13–15] In particular, models that focus on the hopping transport in purely disordered organic materials usually consider randomly distributed energy levels, which are described by a Gaussian density of states (DOS). These models turned out to be quite successful and were, as well, translated into simple one-dimensional descriptions and scalar functions for charge-carrier mobility that are applicable in classical drift-diffusion models.[16–19]

Recently, we presented a simulation model that takes advantage of these concepts and is applicable to organic single-carrier devices with symmetrically arranged electrical doped injection layers [p-doped/intrinsic/p-doped (p-i-p) and n-doped/intrinsic/n-doped (n-i-n) structures].[20] It is based on a master-equation approach for the extended Gaussian disorder model (EGDM) by Coehoorn *et al.*,[19] which describes the hopping transport in purely disordered organic materials assuming a Gaussian DOS with uncorrelated site energies. The model is consistent with the carrier density and field dependence of mobility as derived by Pasveer *et al.*[16] We showed how this model can be applied to the quantitative determination of energy barriers in p-i-p structures with multiple intrinsic layers, and pointed out that this concept may be used as well for the analysis of charge-carrier transport in more complex devices such as OLEDs. In this paper, this shall be demonstrated on a white OLED with fluorescent blue and phosphorescent red and green emission. We will simulate and interpret a series of p-i-p and n-i-n devices that contain parts of the layer sequence in the OLED. These devices reconstruct the OLED layer sequence step by step and cover all layers and interfaces in the OLED. The goal is to determine the transport-level profiles for holes and electrons.

II. SIMULATION MODEL

We present a simulation model that is applicable to organic single-carrier devices with electrical doped injection layers (p-i-p and n-i-n structures). These devices are beneficial for a numerical analysis because they show Ohmic contacts[7] at the electrodes as well as zero built-in voltage. We base our model on a one-dimensional (1D) master-equation description of the EGDM by Coehoorn *et al.*[19] This 1D description of the EGDM has been derived from three-dimensional (3D) simulations, which assume a Gaussian DOS (described by parameters N_{st} and σ) with uncorrelated site energies (E)

$$N_{\text{hopping}}(E) = \frac{N_{st}}{\sqrt{2\pi\,\sigma^2}} \exp\left(-\frac{E^2}{2\sigma^2}\right), \tag{1}$$

and describe charge-carrier hopping by Miller-Abrahams rates[21] as a thermally assisted tunneling process. The derived 1D model represents a projection of the transport in the disordered energy landscape to a discrete transport level. It is consistent with the scalar EGDM mobility as derived by Pasveer *et al.*[16] The EGDM mobility is described as a function of temperature (T), electric field (F), and charge-carrier concentration (p). It is commonly written as

$$\mu(p,T,F) = \mu_0(T) \times f(F) \times g(p), \tag{2a}$$

where

$$\mu_0(T) = \mu_0^* \exp[-C\,\hat{\sigma}^2], \tag{2b}$$

$$f(F) = \exp\left[0.44(\hat{\sigma}^{3/2} - 2.2) \times \left(\sqrt{1 + 0.8\left(\frac{Fea}{\sigma}\right)^2} - 1\right)\right], \tag{2c}$$

$$g(p) = \exp\left[\tfrac{1}{2}(\hat{\sigma}^2 - \hat{\sigma})(2\,p\,a^3)^{\delta}\right], \tag{2d}$$

and

$$\delta = 2\,[\ln(\hat{\sigma}^2 - \hat{\sigma}) - \ln(\ln 4)]/\hat{\sigma}^2. \tag{2e}$$

In this description, μ_0^* denotes the mobility in the zero-field and zero-density limits. C is a constant that influences the temperature dependence, and it is expected to take values close to 0.42.[16,17,19,22] The dimensionless DOS width $\hat{\sigma} = \sigma/k_B T$ is the parameter with the most significant influence on the carrier density and field dependence of the mobility. a is determined by the total density of hopping sites: $N_{st} = 1/a^3$.

In comparison to the scalar EGDM description by Pasveer [as given in Eq. (2)], the 1D master-equation model by

Coehoorn is closer to the precedent 3D description because the discretization is chosen in accordance with the density of states. That means that the discretization points can be associated with the molecules and the real charge-transport sites in the device. The model itself is described as follows: The current density at the interface between adjacent sites i and $i+1$ is expressed as

$$j_{i/i+1} = e\,\zeta\,a(p_i\,r^{+}_{i/i+1} - p_{i+1}\,r^{-}_{i/i+1}), \tag{3a}$$

with the next-neighbor hopping rates

$$r^{+}_{i/i+1} = r^{*}_{i}\,g(p_i)\,\exp\left(+\frac{e\,\zeta\,a\,F_{i/i+1}}{2\,k_B T}\right) \tag{3b}$$

for jumps from site i to site $i+1$, and

$$r^{-}_{i/i+1} = r^{*}_{i+1}\,g(p_{i+1})\,\exp\left(-\frac{e\,\zeta\,a\,F_{i/i+1}}{2\,k_B T}\right) \tag{3c}$$

for jumps in the reverse direction. Therein, ζa denotes the average intersite distance. The expression

$$r^{*}_{i} = \frac{\mu_{0,i}(T)\,k_B T}{(\zeta\,a)^2\,e} \tag{3d}$$

gives the hopping rate in the zero-field and zero-density limits. According to Coehoorn,[19] the parameter ζ has to be chosen such that the master-equation results most optimally meet the field dependence of mobility as described by the $f(F)$ function in Eq. (2c). Therefore, we compare classical drift-diffusion simulations[23] using the EGDM mobility description, as given by Eq. (2), and the master-equation method, as given by Eq. (3). For our devices, we obtain good overall agreement for the two methods with a constant ζ of 1.4.

In our approach, we fully account for the influence of excess charges on the electric field and consider electrical doping by a homogeneous background charge density. The injection from the metal to the organics is described as Ohmic.[24] The transport across organic interfaces is treated with a simple exponential factor, i.e., the hopping rate at an energy barrier with a positive height ΔE is multiplied by a term $\exp(-\Delta E/k_B T)$, whereas the hopping rate in the reverse direction is not changed.[24] This description implies the assumption of a constant transport level within the DOS of the organic materials, which is commonly regarded as valid for charge-carrier concentrations below 1% to 10% of the total density of hopping sites N_{st}.[25] Furthermore, we envisage the possible occurrence of trapping states. We describe the amount of trapped charges with the Fermi-Dirac distribution and a quasi-Fermi level, which is determined by the amount of nontrapped charges. The energetic distribution of trapping sites is described as a superposition of an exponential and a Gaussian DOS:

$$N_{\text{trapping}}(E) = \frac{N_{t,1}}{E_{t,1}}\exp\left(\frac{E}{E_{t,1}}\right) + \frac{N_{t,2}}{\sqrt{2\,\pi\,\sigma^2_{t,2}}}\exp\left(-\frac{(E-E_{t,2})^2}{2\,\sigma^2_{t,2}}\right), \tag{4}$$

with the total density of trapping sites $N_{t,1}+N_{t,2}$ and the characteristic trapping depths $E_{t,1}$ and $E_{t,2}$. This treatment assumes trapped charges to be completely immobile and therefore requires that $N_{t,1}+N_{t,2} \ll N_{st}$.

III. RESULTS AND DISCUSSION

A. OLED description

We analyze the charge-carrier transport in one of the standard designs for white OLEDs. It was presented by Schwartz *et al.*[10] in 2006 and combines *phosphorescent red* {N,N′-di(naphthalen-1-yl)-N,N′-diphenyl-benzidine (NPB) doped with 5 wt% of iridium(III)bis(2-methyldibenzo-[f,h]chinoxalin)(acetylacetonat) [Ir(MDQ)$_2$(acac)]} and *green* {4,4′,4″-tris(N-carbazol-9-yl)-triphenylamine (TCTA) doped with 8 wt% of Tris(2-phenylpyridin)iridium(III) [Ir(ppy)$_3$]} emission layers (ELs) and a *fluorescent blue* EL {2,2′,7,7′-tetrakis(2,2′-diphenylvinyl)spiro-9,9′-bifluorene (Spiro-DPVBi)}. Fluorescent and phosphorescent recombination zones are separated by an ambipolar interlayer (IL) {TCTA and 2,2′,2″-(1,3,5-Phenylen)tris(1-phenyl-1H-benzimidazol) (TPBi) in a mixing ratio of 2:1} with a higher triplet-exciton energy to prevent the diffusion and loss of triplet excitons from the phosphorescent ELs to the nonradiative triplet states of the fluorescent blue emitter. In contrast to the original stack proposed by Schwartz *et al.*,[10] we choose NPB for the electron-blocking layer, 2,4,7,9-tetraphenyl-1,10-phenanthroline (TPPhen) for the hole-blocking layer, 2,7-tetra-(di-p-tolylamine)-9-9-spirobifluorene (Spiro-TTB) doped with 4 wt% of 2,2′-(perfluoronaphthalene-2,6-diylidene)dimalononitrile (F_6-TCNNQ) for the p-doped layer, and TPPhen doped with 4 wt% of tetrakis(1,3,4,6,7,8-hexahydro-2H-pyrimido[1,2-a]pyrimidinato)ditungsten (II) [W_2(hpp)$_4$] for the n-doped layer. TPPhen and W_2(hpp)$_4$ replace 4,7-diphenyl-1,10-phenanthroline (BPhen) and cesium (Cs) in the original stack. The application of a molecular n dopant instead of Cs guarantees high reproducibility of the n-doped layer, which is crucial to the comparability of different devices. The other materials have been introduced to the OLED stack to obtain higher thermal stability and a purely amorphous structure (important to the simulation model). The complete OLED stack including layer thicknesses is sketched in Fig. 1.

The OLED is designed for standard illuminant A, as defined by the Commission Internationale de l'Éclairage (CIE). Figure 1 shows the CIE coordinates of two different OLED samples with IL thicknesses of 3 and 5 nm. The CIE coordinates of both devices are close to the black-body line, and the IL thickness seems to affect the ratio of fluorescent blue to phosphorescent red and green emission. Aside from the color coordinates, another interesting point is the OLED efficiency. First of all, we try to estimate the external quantum efficiency (EQE) from some simple considerations. For this, we assume 100% electrical efficiency, intrinsic radiative efficiencies of 80% for the phosphorescent[26,27] and 20% for the fluorescent emitters. The outcoupling efficiency of the OLED has been evaluated to 1/5 by optical simulations.[28] Furthermore, we assume that the recombination is homogeneous over the emission layers. Hence, our estimated EQE is $1/5 \times (80\% + 80\% + 20\%)/3 = 12\%$. By comparison, experimentally (in a goniometer) we observe considerably lower efficiencies of 8.9% for the OLED with the 3-nm-thick IL and of only 5.4% for the OLED with the 5-nm-thick IL. Aside from the fact that the measured efficiencies are lower than expected,

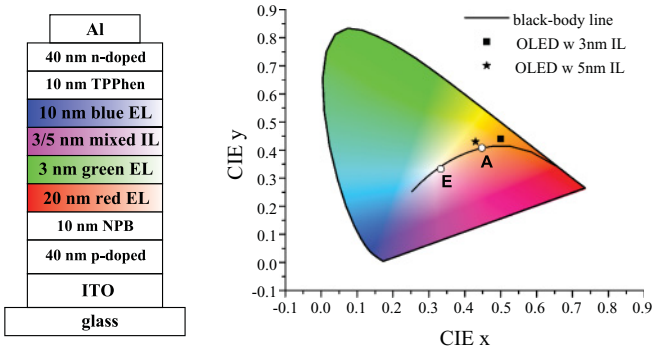

FIG. 1. (Color online) On the left: Sequence of organic layers in the white OLED under investigation. The fluorescent blue emission layer (EL) is separated from the phosphorescent green and red emission layers by an ambipolar interlayer (IL). On the right: Dependence of color coordinates on the IL thickness, illustrated in the xy color space as defined by the Commission Internationale de l'Éclairage (CIE). The color coordinates of two OLEDs with IL thicknesses of 3 and 5 nm are shown to be close to the CIE standard illuminant A and close to the black-body line. The shift of color coordinates observed along the black-body curve indicates that the IL thickness affects the ratio of fluorescent to phosphorescent emission.

it is somewhat astonishing that the OLED efficiency depends so tremendously on the IL thickness. One could argue that this may be explained by the shift in the color coordinates, from inefficient fluorescent to more efficient phosphorescent emission. However, this should not have such a drastic effect. At maximum, the recombination could shift completely onto the phosphorescent emitters. Then, no inefficient blue emission would be left and the efficiency would increase by a factor of $(80\% + 80\% + 80\%)/(80\% + 80\% + 20\%) = 4/3$. By comparison, 8.9/5.4 is 1.65 and hence considerably larger than 4/3. This suggests that there is another efficiency-loss mechanism in the IL between the fluorescent and phosphorescent recombination zones. In our numerical study, we will try to clarify this loss mechanism.

As already mentioned, we intend to determine the transport-level profiles for holes and electrons in the OLED. Therefore, we build various p-i-p and n-i-n devices by thermal evaporation on precoated indium tin oxide (ITO) substrates under ultrahigh vacuum conditions. Aluminum (Al) is used as top contact (cathode). The layer sequences and labels of the devices are given in Table I. The devices reconstruct the OLED layer sequence step by step and cover all layers and interfaces.

Before attempting a numerical analysis of their current-voltage (IV) characteristics, we investigate the different organic layers by UV-photoelectron spectroscopy (UPS), performed with a Phoibos100 system [Specs, Berlin, Germany (see Ref. 29 for details)]. Therefore, we prepare organic single layers of 10 nm thickness on silver and gold substrates. Figure 2(a) illustrates the results. The binding energy is in reference to the vacuum level. UPS measurements are commonly used to determine ionization potentials and highest occupied molecular orbital (HOMO) levels. In experimental physics, HOMO levels are often associated with the levels of charge-carrier transport, and changes in HOMO level with energy barriers. Similarly, theoretical models for transport in disordered organic materials, such as the EGDM, assume a

TABLE I. A summary of the single-carrier devices studied to analyze the hole and electron transport in the white OLED. The table provides the sequence of intrinsic layers in these devices, starting from the anode side. The standard thickness for the surrounding p-doped Spiro-TTB and n-doped TPPhen layers is 50 nm, except for device $rgmb_p$, where we use 40 nm as in the analyzed OLED device. The letters used to label the devices shall be associated with the *red* [NPB:Ir(MDQ)$_2$(acac) (5 wt%)], *mixed* [TCTA:TPBi (2:1)], *green* [TCTA:Ir(ppy)$_3$ (8 wt%)], and *blue* (Spiro-DPVBi) layers in the OLED. a, b, c represent hypothetical layers with different transport properties used for a theoretical study on the insertion of a layer into a p-i-p device. The numbers used in the device labels refer to varied layer thicknesses, e.g., $rg1_p$ and $rg2_p$ refer to devices with thicknesses of 10 and 20 nm for the green emission layer.

p-i-p devices	
1_p	100 nm NPB
2_p	200 nm NPB
$a1_p$	20 nm NPB/20 nm a/60 nm NPB
$a2_p$	20 nm NPB/40 nm a/40 nm NPB
$b1_p$	20 nm NPB/20 nm b/60 nm NPB
$b2_p$	20 nm NPB/40 nm b/40 nm NPB
$c1_p$	20 nm NPB/20 nm c/60 nm NPB
$c2_p$	20 nm NPB/40 nm c/40 nm NPB
r_p	10 nm NPB/20 nm red/50 nm NPB
$rg1_p$	10 nm NPB/20 nm red/10 nm green/40 nm NPB
$rg2_p$	10 nm NPB/20 nm red/20 nm green/30 nm NPB
rgm_p	10 nm NPB/20 nm red/10 nm green/5 nm mixed/35 nm NPB
$rgmb_p$	10 nm NPB/20 nm red/3 nm green/3 nm mixed/10 nm blue/10 nm NPB
$rm1_p$	10 nm NPB/20 nm red/10 nm mixed/40 nm NPB
$rm2_p$	10 nm NPB/20 nm red/20 nm mixed/30 nm NPB
$rb1_p$	10 nm NPB/20 nm red/10 nm blue/40 nm NPB
$rb2_p$	10 nm NPB/20 nm red/20 nm blue/30 nm NPB
n-i-n devices	
1_n	40 nm TPPhen
2_n	60 nm TPPhen
$b1_n$	40 nm TPPhen/10 nm blue/10 nm TPPhen
$b2_n$	30 nm TPPhen/20 nm blue/10 nm TPPhen
$mb1_n$	35 nm TPPhen/5 nm mixed/10 nm blue/10 nm TPPhen
$mb2_n$	30 nm TPPhen/10 nm mixed/10 nm blue/10 nm TPPhen

discrete transport level. As mentioned already in Sec. II, the transport level in a Gaussian DOS is commonly considered at a constant energy if the charge-carrier concentration is below 1% to 10% of the total density of hopping sites. However, *a priori* it is not exactly clear at which energy since the theoretical transport level depends on the form of the DOS and on other parameters such as the inverse localization radius of the charge carriers.[25] Consequently, it is not possible to directly conclude the transport-level profile in the OLED alone from UPS measurements. Nevertheless, the UPS results contain valuable information. In the simulation model, charge-carrier transport is assumed to occur via jumps in a Gaussian DOS, the width of which is the most significant parameter for the carrier density and electric-field dependence of the mobility. Therefore, we fit the UPS results with Gaussian functions to obtain the DOS widths of the organic materials. Certainly, it is arguable

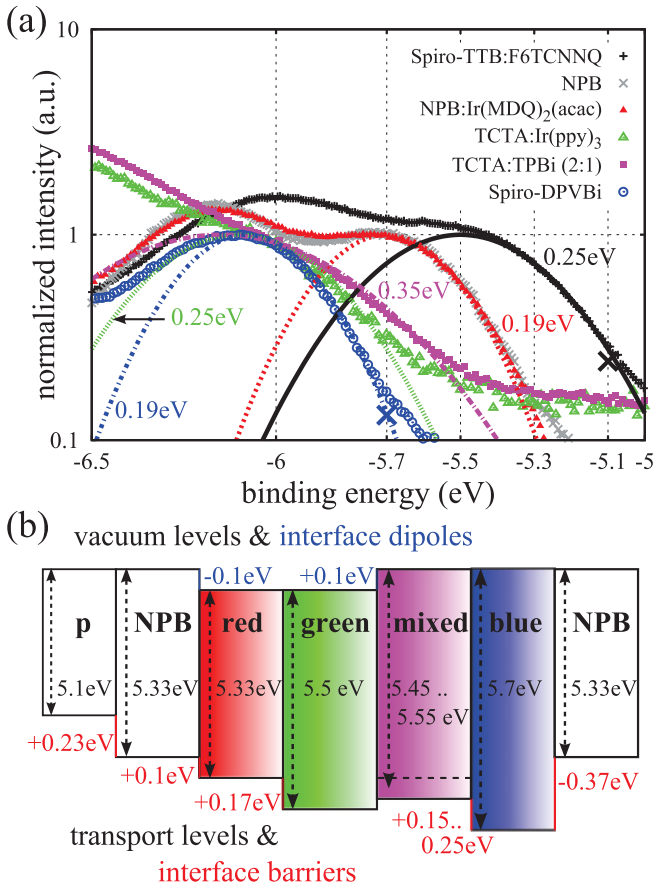

FIG. 2. (Color online) (a) Normalized UPS measurements (points) for the different hole-transporting layers in the white OLED. From the measurements, we derive the DOS widths of the investigated materials by comparing with Gaussian curves (lines). (b) Resulting energy-level profile for hole transport in the white OLED. The scheme illustrates vacuum levels and interface dipoles (blue), as well as transport levels and energy barriers (red), as applied in the numerical simulations for the studied p-i-p devices. The obtained transport levels may also be compared with the UPS measurements above. As an example, we marked the transport levels in the p-doped layer and in the blue EL with large crosses (×).

whether the obtained DOS widths may be used directly to describe the mobilities because the UPS signal is broadened by different effects. First, UPS is a surface-sensitive technique, and at the surface to the vacuum, the dielectric constant changes and electrostatic screening effects may occur. This should affect the correlation in site energies and, consequently, the width of the DOS. Second, immanent features of the organics, such as vibronic modes of the ionized molecules, should contribute to broaden the UPS signal. The EGDM itself does not account for correlation in site energies, and recent publications[18,22] have shown that this can be compensated by an effectively enlarged DOS width in combination with a reduced state density N_{st}. Therefore, it seems straightforward to directly apply the measured DOS widths and to adjust the parameter N_{st} for the state density in an effective way. Moreover, the application of measured DOS widths in the numerical analysis is attractive because it will allow us to visualize the resulting transport levels in the UPS scans.

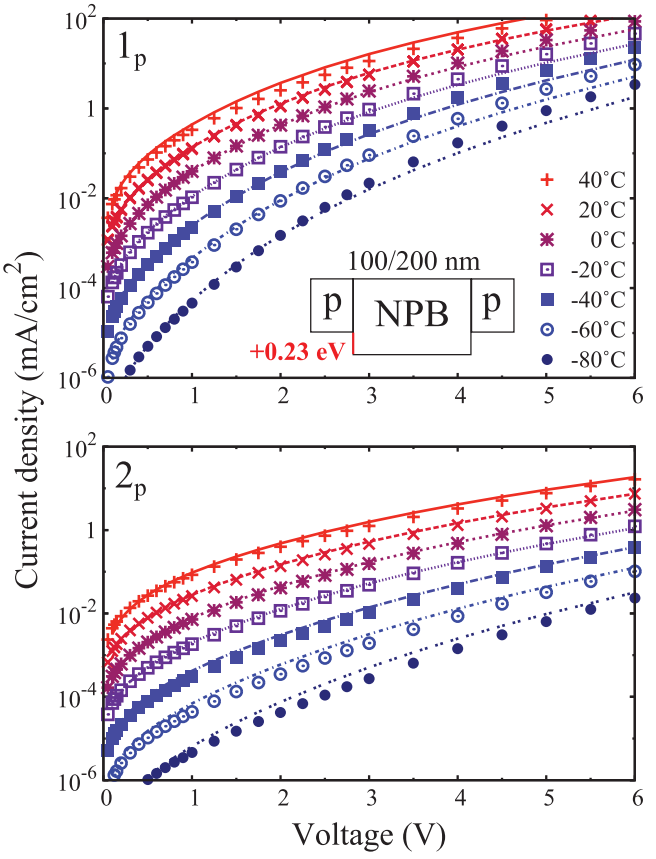

FIG. 3. (Color online) Experimental (points) and simulated (lines) IV characteristics of p-i-p devices 1_p and 2_p. The devices contain 100 and 200 nm of NPB between p-doped layers of Spiro-TTB. The numerical analysis allows us to determine the transport parameters for the two different organic layers and shows that the rising distance between curves of successive temperatures indicates a freeze-out of active dopants.

B. p-i-p devices with single intrinsic layers

We have measured the IV characteristics of devices 1_p and 2_p with 100 and 200 nm of NPB between 50-nm p-doped layers of Spiro-TTB in a temperature-controlled environment at temperatures from −80 °C to +40 °C. For the fit of experimental results in Fig. 3, we apply a DOS width of 0.247 eV for p-doped Spiro-TTB and of 0.19 eV for NPB [in agreement with the Gaussian curves in Fig. 2(a)], and a constant state density of 10^{20} cm^{-3}. The state density is about one order of magnitude smaller than estimated from the molar mass and density of the materials. This discrepancy may be ascribed to our direct application of measured DOS widths and the neglect of correlation in site energies within the EGDM.[18,22] At the interface between the p-doped layer and NPB, we assume vacuum-level alignment and adjust the energy barrier to +0.23 eV, which meets transport levels, e.g., at −5.1 eV in the p-doped layer and at −5.33 eV in the NPB layer [as illustrated in Fig. 2(b)]. The concentration of active dopants in the p-doped layers is assumed to be 2×10^{17} cm^{-3} for temperatures above −20 °C, and $(1.9, 1.7, 1.3) \times 10^{17}$ cm^{-3} at −40 °C, −60 °C, and −80 °C. The freeze-out of dopants has to be considered in the simulations because the distance

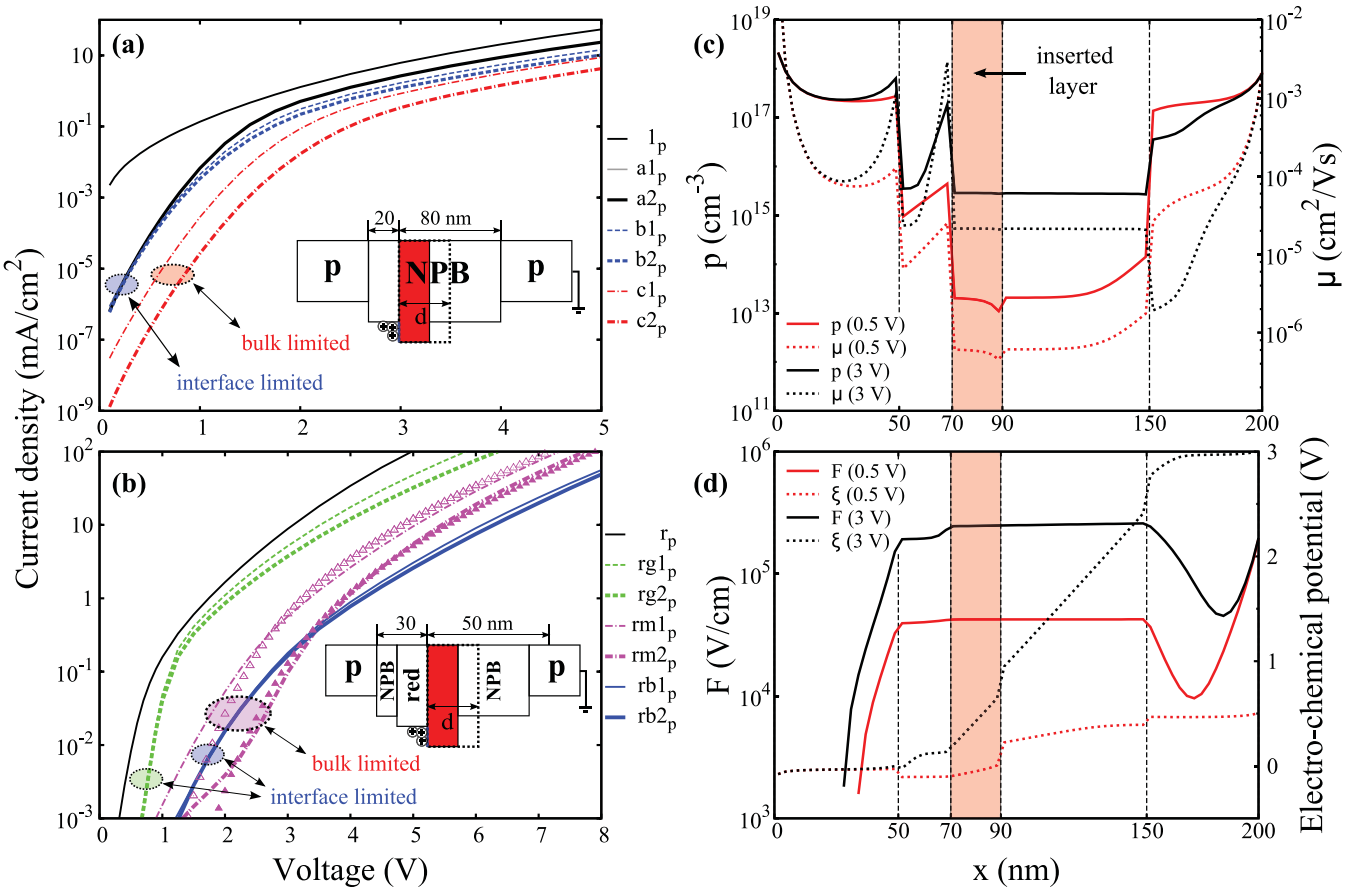

FIG. 4. (Color online) (a) Theoretical study on the insertion of three layers a, b, c with different transport properties (summarized in Table II) into p-i-p device 1_p. For each of these layers, we consider thicknesses of 20 (label 1) and 40 nm (label 2). The dependence of the IV characteristics on the thickness of the inserted layer in the low-voltage regime allows us to discern strong current-limiting factors such as trap states in the bulk of the inserted layer (attributed to layer c) from the limitation by the energy barrier at the interface to the inserted layer (attributed to all inserted layers). (b) Measured IV characteristics of 7 p-i-p devices (lines) for the analysis of hole transport in the white OLED. The measurements reveal limitation of hole transport at the interface between the red and green EL and in the bulk of the mixed IL. The energy barrier, which forms at an interface between the red and blue EL, appears larger than the barrier between the red and green EL. The triangles (△,▲) represent simulations for the devices $rm1_p$ and $rm2_p$, and assume deep trap states around the middle of the band gap in the mixed IL. (c) Hole concentration (left scale, solid curves) and mobility (right scale, dashed curves) vs position in device $a1_p$ at 0.5 V (red) and 3 V (black). (d) Electric field (left scale, solid curves) and electrochemical potential (right scale, dashed curves) vs position in device $a1_p$ at 0.5 V (red) and 3 V (black).

between the IV curves of successive temperatures becomes wider at small temperatures, which can not be explained by the temperature dependence of the mobility in the EGDM. To reproduce this behavior, we also consider different scenarios including charge-carrier trapping and non-Ohmic injection from the anode to the p-doped layer. However, a freeze-out of dopants is the only explanation that gives satisfying fits for both devices. For simplicity, we restrict further IV measurements to the temperature range from −20 °C to +40 °C where the concentration of active dopants can be regarded as constant.

C. Identifying trap states

Having established a numerical description for p-i-p devices with p-doped layers of Spiro-TTB comprising single intrinsic layers of NPB, we focus now on the ELs and the mixed IL in the OLED. The idea is to insert these layers into the intrinsic NPB layer one after another. Before analyzing experimental results, we first want to study theoretically the insertion of a layer into a p-i-p device, based on the parameters obtained for p-doped Spiro-TTB and intrinsic NPB at 20 °C. Therefore, we consider three hypothetical layers a, b, c, which shall replace parts of the intrinsic NPB layer in device 1_p, as sketched in the inset of Fig. 4(a). We choose two different thicknesses, 20 and 40 nm, for each of these layers and refer to them with labels 1 and 2. To the interface between NPB and the inserted layer, we attribute an energy barrier of 0.23 eV for each of the three layers, which is the same energy barrier as between the p-doped layer and NPB. The three layers shall differ in terms of mobility and trap distribution. The parameters are summarized in Table II.

The *first* inserted layer a has the same mobility as NPB and contains no traps. As illustrated in Fig. 4(a), the energy barrier at the interface to the inserted layer considerably affects the IV characteristics and leads to reduced currents. Moreover, we notice that this limitation becomes less significant at higher

TABLE II. A summary of transport parameters applied in the numerical analysis of hole transport in the white OLED. The first three parameter sets a, b, c are applied in the theoretical study on the insertion of a layer into the intrinsic region of p-i-p device 1_p. The following parameter sets describe the hole-transporting layers in the white OLED. In our analysis, we find different possible parameter sets for the mixed IL in the OLED (labeled as IL_1 and IL_2).

	N_{st} (cm^{-3})	σ (eV)	μ_0^* (cm^2/Vs)	C	$N_{t,1}$ (cm^{-3})	$E_{t,1}$ (eV)
a	10^{20}	0.190	3	0.34	0	0
b	10^{20}	0.247	800	0.45	0	0
c	10^{20}	0.247	800	0.45	10^{17}	1.0
p-doped	10^{20}	0.247	800	0.45	0	0
NPB	10^{20}	0.190	3	0.34	0	0
Red EL	10^{20}	0.190	0.6	0.34	0	0
Green EL	10^{20}	0.247	800	0.45	0	0
Mixed IL$_1$	10^{20}	0.350	3×10^3	0.47	0	0
Mixed IL$_2$	10^{20}	0.350	60×10^3	0.47	2×10^{17}	1.0
Blue EL	10^{20}	0.190	0.6	0.34	0	0

bias voltages. For instance, at 0.5 V, the IV characteristics of devices 1_p and $a1_p$ differ by almost three orders of magnitude, but they become nearly identical for voltages above 2 V. This behavior is explained by the charge-carrier dependence of the mobility [illustrated in Fig. 4(c)]: At *low bias*, there is sufficient thermal injection from the p-doped layer to the intrinsic NPB layer (over the energy barrier at the first interface in the device), and the current is limited by the energy barrier at the interface to the inserted layer (second interface in the device), which is apparent because of the low charge-carrier concentration in the third layer behind the second interface. At *higher bias*, the mobility in front of the second interface is enhanced due to increased charge-carrier concentration. Therefore, the transport across the energy barrier to the inserted layer is facilitated, resulting in equal charge-carrier concentrations behind the two interfaces and the limitation of current by the first interface. Thus, the insertion of a layer into the intrinsic region of a p-i-p device modifies the IV characteristics predominantly at low bias and becomes less significant at higher bias voltages. Furthermore, we notice that the IV characteristics of devices $a1_p$ and $a2_p$ are independent from the thickness of the inserted layer (for positive bias). The reason is that, in the region from the accumulated holes in front of the inserted layer up to the depletion zone of the following p-doped layer, the electric field is at its maximum in the device and nearly constant [Fig. 4(d) shows the electric field profile in device $a1_p$ at 0.5 and 3 V]. This dominates the voltage loss in the devices $a1_p$ and $a2_p$ at low bias, and explains their similar IV characteristics because the distance from the left interface of the inserted layer to the depletion zone of the following p-doped layer is the same in both devices.

The *second* inserted layer b also contains no traps but has a lowered mobility, described with the parameters of p-doped Spiro-TTB. The lowered mobility mainly influences the high-voltage regime and leads to slightly reduced currents and to a marginal dependence on the thickness of the inserted layer. At low bias, the deviations from the characteristics of the devices $a1_p$ and $a2_p$ are negligible. This means that the influence of the energy barrier on the IV characteristics in this regime is not smeared out by the mobility, which is important as we want to determine the energy barriers from the IV characteristics.

The *third* inserted layer c has the same properties as material b, but additionally contains trap states, described by an exponential trap distribution ($N_{t,1} = 10^{17}$ cm^{-3}, $E_{t,1} = 1$ eV) with a density close to the concentration of active p-dopants in Spiro-TTB (2×10^{17} cm^{-3}). In comparison to the devices $b1_p$ and $b2_p$, the currents are considerably reduced at low bias due to a changing quasi-Fermi level and the filling of trap states. At higher voltages, the quasi-Fermi level rises less and the filling of trap states saturates. Therefore, the currents become similar to those of devices $b1_p$ and $b2_p$. In the regime where the traps are filled, a clear dependence on the thickness of the inserted layer is observable. Consequently, it is possible to conclude from a thickness variation of the inserted layer whether there are strong current-limiting factors such as trap states in the bulk of the inserted layer.

It is particularly important to identify trapping states in the OLED since the parameters describing the trap states are usually numerous, correlated with the other simulation parameters, and hence difficult to determine. Figure 4(b) shows the IV characteristics of devices that were fabricated to analyze the green and blue EL as well as the mixed IL in the white OLED for hole-trapping states. The layer sequences of the devices are given in Table I. The reference p-i-p device r_p comprises NPB and 20 nm of NPB:Ir(MDQ)$_2$(acac) (red EL) between p-doped Spiro-TTB layers. The devices rg_p and rb_p additionally contain inserted layers of TCTA:Ir(ppy)$_3$ (green EL) and Spiro-DPVBi (blue EL), respectively. At low bias, the devices show lower currents in comparison to the reference device r_p, and no dependence on the thickness of the inserted layer is observed, which clearly demonstrates the limitation of the current by energy barriers at the interface between the red and green EL in device rg_p, and at the interface between the red and blue EL in device rb_p. It is also apparent that the energy barrier to the blue EL is larger, which indicates a lower transport level in Spiro-DPVBi in comparison to TCTA:Ir(ppy)$_3$. By contrast, the devices with the mixed IL of TCTA:TPBi ($rm1_p$ and $rm2_p$) show a strong dependence on the thickness of the inserted layer, which demonstrates the

presence of hole-trapping states in the IL. As the separation of the IV characteristics for the devices $rm1_p$ and $rm2_p$ is broad only in a small bias range, the trap states are likely to be of considerable depth. Furthermore, because of the higher currents in device $rm1_p$ in comparison to the devices $rb1_p$ and $rb2_p$ at low bias, the transport level of the mixed TCTA:TPBi layer is expected to be above the transport level in Spiro-DPVBi.

D. Deriving the hole-transport level profile

With the acquired knowledge, we go on with the numerical analysis of hole transport in the OLED. The layer next to the intrinsic NPB layer is the *red* EL. Our UPS measurements [Fig. 2(a)] show the same ionization potential and DOS width for pure NPB and NPB:Ir(MDQ)$_2$(acac). However, we observe a dipole of -0.1 eV at the interface between the two layers,[29] as illustrated in Fig. 2(b). Therefore, we assume an equivalent energy barrier of $+0.1$ eV for hole transport at this interface in device r_p, which contains 20 nm of the red EL in the intrinsic region, and achieve accurate IV simulations for positive and negative bias voltages at temperatures from $-20\,^{\circ}$C to $+40\,^{\circ}$C (Fig. 5). Herein, we apply for the red EL a slightly lower mobility in comparison to pure NPB, which has only marginal influence on the simulated IV curves of device r_p but is beneficial to accurately describe the hole transport across the third interface in the white OLED, between the red and green EL. The simulation parameters for device r_p are summarized in Table II and in the device scheme on the top-right corner of Fig. 5.

In our UPS measurements [Fig. 2(a)], the *green* EL shows the same DOS width as the p-doped Spiro-TTB layer. Therefore, we essay to apply the same mobilities for both layers and to solely adjust the energy barrier between the red and green EL in our simulations for the devices $rg1_p$ and $rg2_p$ (Fig. 5), which additionally contain 10 and 20 nm of the green EL next to the red EL in the intrinsic region. Between the two ELs, we assume an energy barrier of $+0.17$ eV and vacuum-level alignment. Due to the similarity of the phosphorescent red and green emitters, the dipole effect at the interface between NPB and the red EL is assumed to recur at the interface between the green EL and NPB [see the resulting energy level profile in Fig. 2(b) for clarity]. As the simulations agree well with the experimental results for both devices, these assumptions seem to be justified.

In the OLED layer sequence, the green EL is followed by the *mixed* IL of TCTA:TPBi (2:1). As discussed above, we expect hole-trapping states in this layer. However, in first simulations for device rgm_p, which additionally contains 5 nm of the mixed IL next to the green EL in the intrinsic region, we neglect trap states and obtain good fits (illustrated in Fig. 6) assuming energy barriers of -0.05 eV at the interface between the green EL and the mixed IL (fourth interface in the OLED), and of -0.22 eV at the interface between the mixed IL and NPB. Estimating an interface dipole of $+0.1$ eV at the fourth interface and vacuum-level alignment between the mixed IL and NPB, we obtain the transport level in the mixed IL at -5.55 eV below the vacuum level (continuing with the reference transport level in the p-doped layer at -5.1 eV below the vacuum level). This is slightly lower than the resulting transport level in the green EL at -5.5 eV below the vacuum level. By contrast, a look on the UPS results in Fig. 2(a) rather suggests that the transport level in the mixed IL may be situated a bit closer to the vacuum level in comparison to the green EL. In our theoretical study on the insertion of a layer in the intrinsic region of a p-i-p device (Sec. III C), we have mentioned that, in the case of trap states, the parameters describing the trap distribution are usually correlated with the other simulation parameters. This means that normally it is not possible to unambiguously extract the energy barrier to an inserted layer when trap states occur in this layer. Here, the neglect of trapping states in the mixed IL leads to a lower transport level as when traps are taken into account. To examine this deviation, we introduce an additional exponential trap distribution to the mixed IL, with a total density of trapping sites $N_{t,1} = 2 \times 10^{17}$ cm^{-3} and a characteristic trapping depth $E_{t,1} = 1.0$ eV. With these parameters for the trap distribution in the mixed IL, we obtain the best simulation results (illustrated in Fig. 6) with an energy barrier of -0.12 eV at the interface between the mixed IL and NPB, and with a 20 times higher mobility in the mixed IL in comparison to the trap-free case (see Table II). The optimized energy barrier of -0.12 eV coincides with a transport level in the mixed IL at -5.45 eV below the vacuum level, which is 0.1 eV higher than in the trap-free case. We observe that different parameters for the trap distribution lead to similar good simulation results, which, in principle, allows us to shift the transport level in the mixed IL arbitrarily. However, best fits were obtained with transport levels between -5.55 and -5.45 eV below the vacuum level. Higher transport levels cause stronger deviations, especially in the low-bias regime. Thus, the proposed parameters for the trap distribution somehow represent the highest acceptable trapping strength in the mixed IL, and should not be understood as absolute.

The last layer in the white OLED with relevance to hole transport is the *blue* EL. The measured DOS width of this layer is the same as for the red EL (0.19 eV), and the UPS measurements in Fig. 2(a) show that it has the highest ionization potential of all layers. The layer is considered as trap free and its mobility parameters are not very significant in the simulations of device $rgmb_p$, which contains all the hole-transporting layers with the actual layer thicknesses of the analyzed OLED device. For simplicity, we use the mobility parameters of the red EL for the blue EL and optimize its transport level, assuming vacuum-level alignment at the interfaces to the mixed IL and to NPB. The optimized transport level is at -5.7 eV below the vacuum level. The simulated IV characteristics of device $rgmb_p$, with and without the assumption of trap states in the mixed IL, are illustrated in Fig. 6. The resulting transport-level profile for the hole transport in the OLED is illustrated in Fig. 2(b).

E. Discussion of hole transport

A comparison of Figs. 2(a) and 2(b) shows that the transport levels and energy barriers assumed in the simulations agree well with the energies observed in the UPS measurements. The obtained transport levels range from -5.1 eV in the p-doped layer down to -5.7 eV in the blue EL and lie in the tails of the DOS. However, we have constructed the transport-level

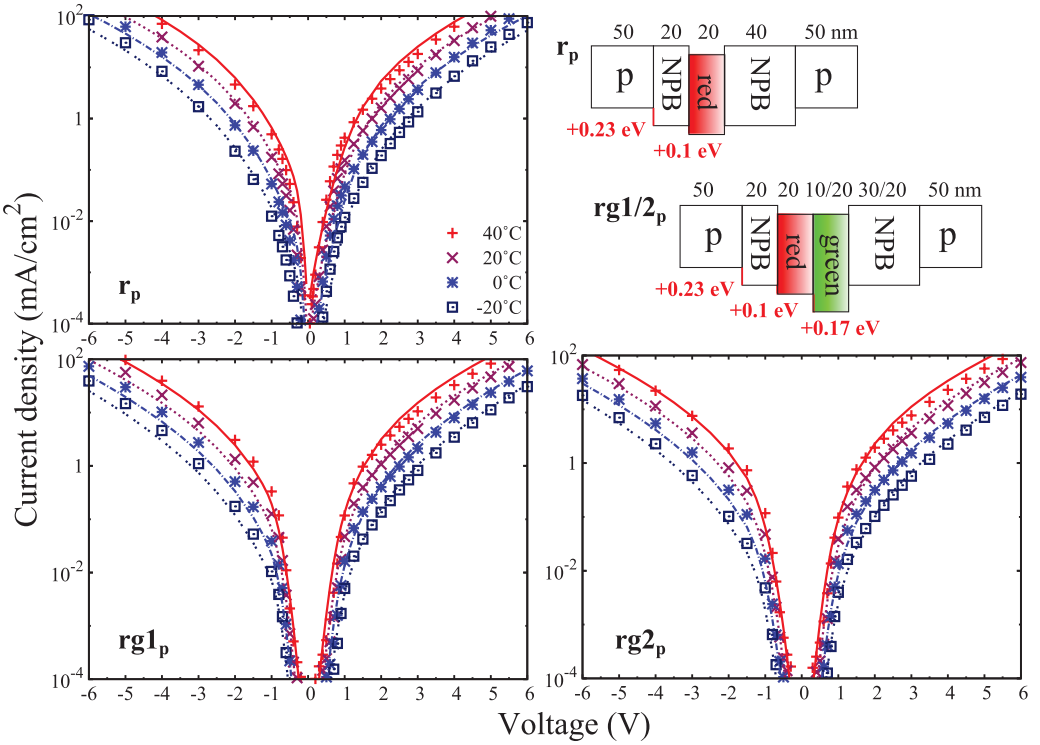

FIG. 5. (Color online) Experimental (points) and simulated (lines) IV characteristics of p-i-p devices r_p, $rg1_p$, and $rg2_p$. The numerical analysis allows us to determine the transport parameters for the red and green EL in the OLED. The applied energy barriers (red) are illustrated in the device schemes on the top right.

profile in reference to the transport level in the p-doped layer at −5.1 eV below the vacuum level, which has been chosen rather arbitrarily. Therefore, the absolute position of the profile could also be shifted. The parameters summarized in Fig. 2(b) and Table II have been consistently applied in all simulations without further variations; they have been established on a number of assumptions and fitting procedures. One of the basic simplifications in our approach is the direct application of UPS scans to determine the DOS widths. This requires, on the one hand, that the energy resolution of the UPS instrument is sufficiently high and, on the other hand, that broadening effects due to immanent features of the investigated layers can be neglected. We have tested the energy resolution of our UPS system on the Fermi edge of metal substrates and could determine the thermal activation energy with an accuracy of 0.01 eV. The same accuracy is assumed for the UPS measurements of the organic layers. Concerning immanent features of the organics, we already mentioned that vibronic modes of the ionized molecules as well as electrostatic screening effects at the surface to the vacuum should broaden the UPS signal. In the presented simulation series, we compensated these broadening effects with an effectively adjusted state density N_{st}, which is about one order of magnitude lower than estimated from the molar mass and density of the materials, and which could be kept constant for all materials. However, we experienced that the DOS width has a rather strong influence on the simulation results, especially for the outer layers of the investigated p-i-p devices. The reason is that it largely influences the charge carrier and electric-field dependence of mobility, which is important to describe the current over energy barriers at interfaces where charges accumulate. This means that the resulting energy barriers are not independent from the applied DOS widths, and it might as well be possible to describe the discussed IV characteristics with a narrower transport-level profile and narrower DOS widths. Nevertheless, the direct application of measured DOS widths works out well and is very convenient. It allows us to consistently describe all our p-i-p devices and to visualize the transport levels directly in the UPS scans.

Furthermore, we demonstrated that transport levels can only be extracted unambiguously from the IV characteristics when the layers are free from trapping states. We showed that it is possible to identify trap states by analyzing how the IV characteristics depend on the layer thickness, and identified trapping states in the mixed IL between the fluorescent and phosphorescent recombination zones. In our analysis, we introduced to this layer an exponential trap distribution with a relatively moderate trapping strength ($N_{t,1} = 2 \times 10^{17}$ cm^{-3}, $E_{t,1} = 1.0$ eV). However, we think that this description is only appropriate for small IL thickness ($\leqslant 5$ nm). For larger IL thickness, we encountered a stronger trapping strength. For instance, the samples $rm1_p$ and $rm2_p$ with 10 and 20 nm of the mixed IL next to the red EL have been simulated with a combined exponential and Gaussian trap distribution ($N_{t,1} = 5 \times 10^{17}$ cm^{-3}, $E_{t,1} = 0.75$ eV, $N_{t,2} = 6 \times 10^{17}$ cm^{-3}, $E_{t,2} = 1.5$ eV, $\sigma_{t,2} = 0.75$ eV). The simulations are illustrated in Fig. 4(b) with triangles. For these devices with large IL thickness, the trapping strength seems to be much higher than before in the samples rgm_p and $rgmb_p$

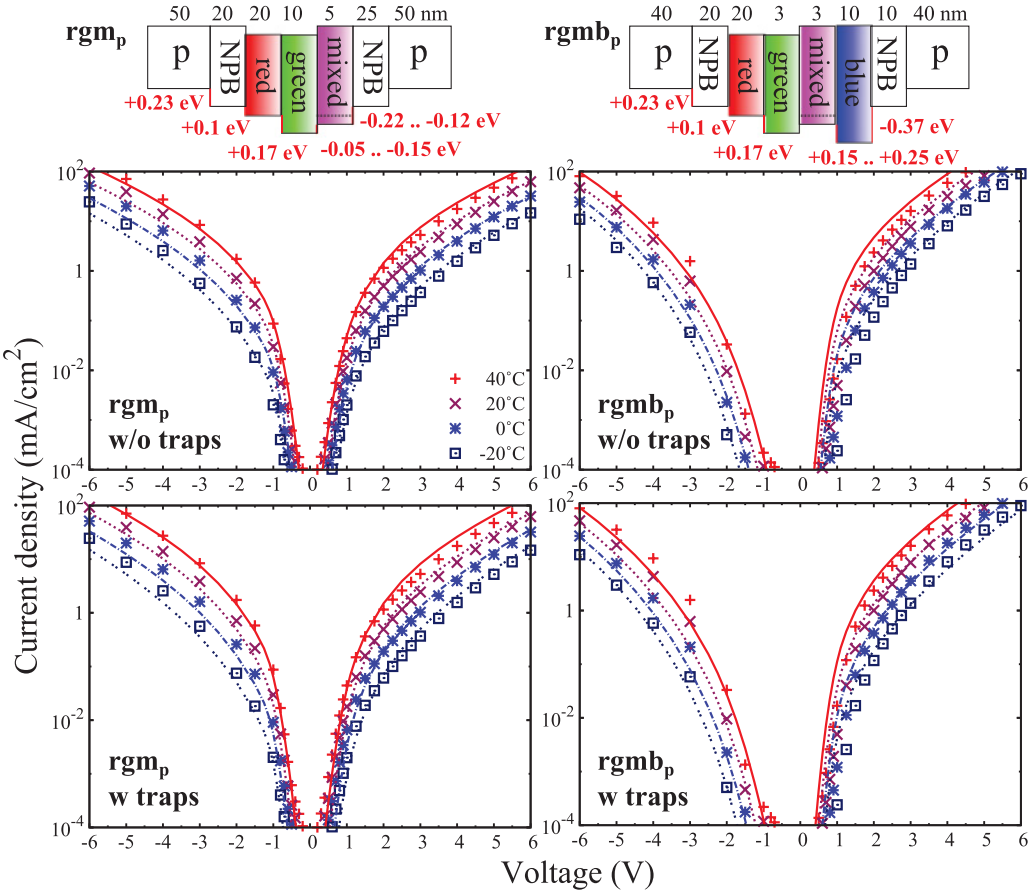

FIG. 6. (Color online) Experimental (points) and simulated (lines) IV characteristics of p-i-p devices rgm_p and $rgmb_p$. The numerical analysis allows us to determine the transport parameters of the mixed IL and the blue EL in the OLED. The applied energy barriers (red) are illustrated in the device schemes on the top. Both devices can be simulated with (w) and without (w/o) traps in the IL, which leads to an ambiguous transport level in this layer.

with thinner ILs. Possible reasons could be the morphology of the mixed IL, the layer might not be smooth enough, or the fact that only a single Gaussian is considered for the charge transport. Particularly interesting is that a considerable amount of deep trap states had to be introduced in the simulations because such trap states represent a path for nonradiative recombination.

F. Comparative analysis of hole and electron transport

Finally, we analyze the electron transport in the OLED in a series of n-i-n devices with n-doped layers of TPPhen. The main problem for this analysis is that we hardly know anything about the lowest unoccupied orbital levels (LUMOs) and the DOS widths. Therefore, we intend to do the analysis in a comparative way, meaning that we start with the already known parameters of the equivalent hole-transporting layers and see whether they are also suitable to describe electron transport.

The first electron-only devices 1_n and 2_n contain single intrinsic TPPhen layers of 40 and 60 nm; their IV characteristics are illustrated on the left side of Fig. 7. In the simulations, we apply the parameters of the p-doped Spiro-TTB layer to the n-doped TPPhen layer, and the parameters of NPB to the intrinsic TPPhen layer (as summarized in Table II). To meet the experimental results, we additionally have to introduce an exponential trap distribution ($N_{t,1} = 2 \times 10^{17}$ cm^{-3}, $E_{t,1} =$ 0.6 eV) to all of the layers in the n-i-n sequence. The energy barrier between the n-doped and the intrinsic layers is set to +0.05 eV. With these assumptions, we obtain very good fits in a temperature range from $-20\,^{\circ}$C to $+40\,^{\circ}$C, as illustrated in Fig. 7. The small energy barrier and the presence of trap states makes the IV characteristics change quite drastically with the thickness of the intrinsic TPPhen layer, which is the reason why we chose the intrinsic layers thinner in comparison to hole transport. The fact that the simulations show the correct temperature dependence is somewhat fortunate, but indicates that the electron-transporting and their equivalent hole-transporting layers may indeed have a similar DOS.

In a next step, we analyze the devices $b1_n$ and $b2_n$ with inserted blue ELs of 10 and 20 nm. As illustrated in the bottom-right plot of Fig. 7, the insertion leads to drastically reduced currents at small bias voltages. At higher bias, the IV characteristics of devices $b1_n$ and $b2_n$ get close to the reference characteristics of device 2_n. This behavior could be explained by the occurrence of trap states in the blue EL. However, the IV characteristics of devices $b1_n$ and $b2_n$ overlap and do not show a strong dependence on the thickness

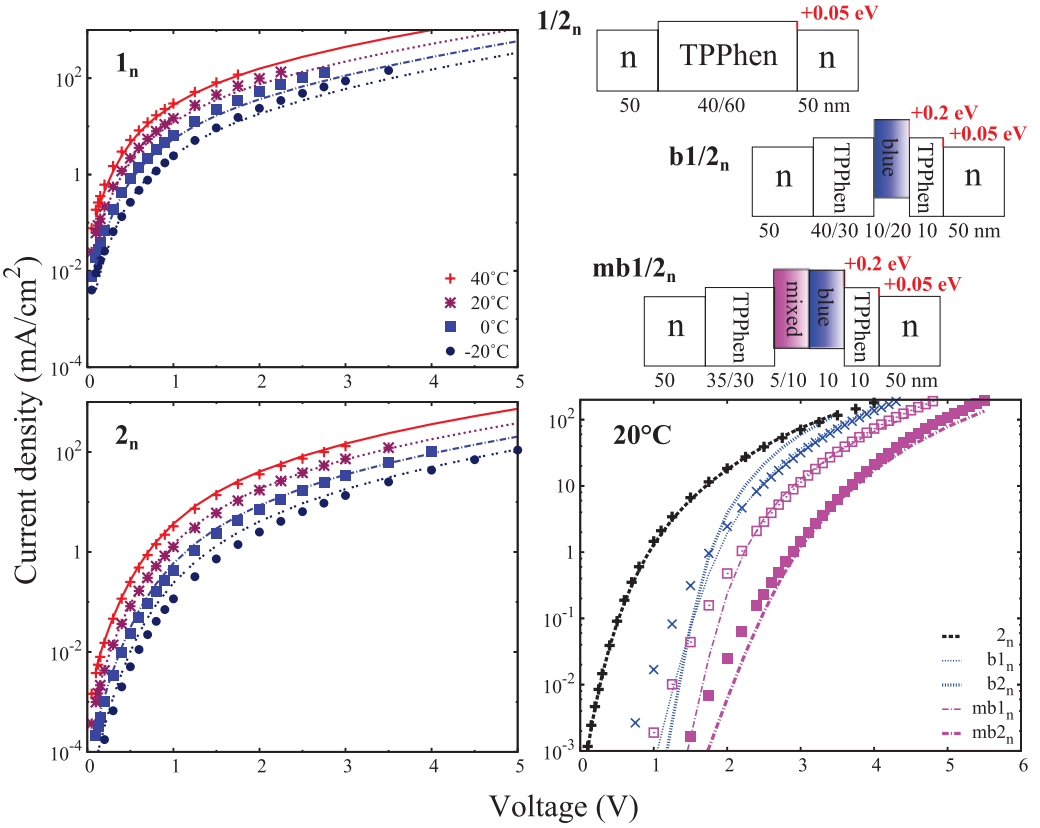

FIG. 7. (Color online) Analysis of electron transport in a series of n-i-n devices. The deduced energy barriers (red) are illustrated in the device schemes on the top right. On the left: experimental (points) and simulated (lines) IV characteristics of n-i-n devices 1_n and 2_n with n-doped and intrinsic layers of TPPhen in a temperature range from $-20\,^{\circ}$C to $+40\,^{\circ}$C. For the simulations, we use the mobility parameters of the equivalent hole-transporting layers in the OLED (p-doped Spiro-TTB and NPB), vary the energy barrier, and additionally assume trap states in the bulk of the layers. On the bottom right: experimental (lines) and simulated (points) IV characteristics of n-i-n devices 2_n (as reference), $b1_n$ and $b2_n$ (with 10 and 20 nm of the blue EL), $mb1_n$ and $mb2_n$ (with 5 and 10 nm of the IL) at $20\,^{\circ}$C. The currents appear to be limited at the interface between TPPhen and the blue EL and in the bulk of the mixed IL. For the simulations, we assume considerable amounts of deep trap states at the interface between TPPhen and the blue EL, as well as in the bulk of the mixed IL.

of the blue EL as we would expect when trap states were present in this layer. A way to reproduce this behavior with the simulation is to assume trap states at the interface between TPPhen and the blue EL. Therefore, we attribute to the last discretization point of the TPPhen layer, at the interface to the blue EL, a combined exponential and Gaussian trap distribution ($N_{t,1} = 2 \times 10^{17}$ cm^{-3}, $E_{t,1} = 0.75$ eV, $N_{t,2} = 3 \times 10^{17}$ cm^{-3}, $E_{t,2} = 1.7$ eV, $\sigma_{t,2} = 0.75$ eV). Additionally, we assume an energy barrier of $+0.2$ eV at this interface. To the blue EL, we attribute the mobility parameters of NPB, as applied already to TPPhen, and consider the bulk of the layer as trap free. The resulting simulations (illustrated in Fig. 7 with blue crosses) show no dependence on the thickness of the blue EL and reproduce the experiments quite well. The occurrence of interface trap states may also explain the strangely overlapping IV characteristics of devices $b1_n$ and $b2_n$ because the trap distributions in these devices could vary a bit.

At last, we analyze the devices $mb1_n$ and $mb2_n$ which additionally contain 5 and 10 nm of the mixed IL. We find their IV characteristics to strongly depend on the IL thickness. Thus, we assume again trap states in this layer. In analogy to hole transport, we attribute less traps to the 5-nm IL in device $mb1_n$ ($N_{t,1} = 2 \times 10^{17}$ cm^{-3}, $E_{t,1} = 0.75$ eV, $N_{t,2} = 3 \times 10^{17}$ cm^{-3}, $E_{t,2} = 1.9$ eV, $\sigma_{t,2} = 0.75$ eV) than to the 10-nm IL in device $mb2_n$ ($N_{t,1} = 5 \times 10^{17}$ cm^{-3}, $E_{t,1} = 0.75$ eV, $N_{t,2} = 6 \times 10^{17}$ cm^{-3}, $E_{t,2} = 1.9$ eV, $\sigma_{t,2} = 0.75$ eV). As already discussed in Sec. III E, this may be explained by the morphology of the IL or the fact that only a single Gaussian DOS is considered for the charge transport.

In summary, we find in the mixed IL quite similar trap distributions for holes and electrons and considerable amounts of trap states deep in the band gap. These trap states represent a path for nonradiative recombination, reduce the EQE of the OLED, and give a reasonable explanation for the fact that the EQE depends so strongly on the IL thickness, as discussed in Sec. III A.

IV. CONCLUSION

We presented a simulation model for the IV characterization of p-i-p and n-i-n structures, and demonstrated its applicability on the quantitative determination of transport levels in a white light-emitting diode with fluorescent blue and phosphorescent red and green emission. We discussed how to distinguish

the current limitation in the bulk of the organic layers from the limitation at interfaces between different organic layers, and demonstrated that transport levels can only be extracted unambiguously from the IV characteristics when the layers are free from trapping states. We obtained a consistent numerical description for numerous p-i-p and n-i-n devices, as well as valuable clues on the charge-carrier transport in the OLED. We revealed the presence of deep trap states in the mixed IL between the fluorescent and phosphorescent emission zones and thereby found an explanation for the low EQE of the OLED and the strong dependence of the EQE on the IL thickness. Furthermore, we identified dipole effects at the interfaces to the phosphorescent recombination zone, a freeze-out of dopants in the p-doped layer at temperatures below −20 °C, as well as various trapping mechanisms in electron transport.

ACKNOWLEDGMENTS

This work was funded by the European Community's Seventh Framework program under Grant No. 213708 (AEVIOM) and by the BMBF under Contract No. 13N 8855 (R2FLEX). We thank our project partners, in particular, R. Coehoorn, for fruitful discussions, as well as NOVALED and sim4tec for their cooperation.

*matthias.schober@iapp.de

[1] S. Reineke, F. Lindner, G. Schwartz, N. Seidler, K. Walzer, B. Lüssem, and K. Leo, Nature (London) **459**, 234 (2009).
[2] H. Kanno, N. C. Giebink, Y. Sun, and S. R. Forrest, Appl. Phys. Lett. **89**, 023503 (2006).
[3] B. Geffroy, P. l. Roy, and C. Prat, Polym. Int. **55**, 572 (2006).
[4] M. T. Lee, C. H. Liao, C. H. Tsai, and C. H. Chen, Adv. Mater. **17**, 2493 (2005).
[5] J. H. Seo, J. H. Park, Y. K. Kim, J. H. Kim, G. W. Hyung, K. H. Lee, and S. S. Yoon, Appl. Phys. Lett. **90**, 203507 (2007)
[6] T. C. Rosenow, M. Furno, S. Reineke, S. Olthof, B. Lüssem, and K. Leo, J. Appl. Phys. **108**, 113113 (2010).
[7] K. Walzer, B. Maennig, M. Pfeiffer, and K. Leo, Chem. Rev. **107**, 1233 (2007).
[8] L. S. Liao, K. P. Klubek, and C. W. Tang, Appl. Phys. Lett. **84**, 167 (2004).
[9] G. Gu and S. R. Forrest, IEEE J. Sel. Top. Quantum Electron. **4**, 83 (2002).
[10] G. Schwartz, K. Fehse, M. Pfeiffer, K. Walzer, and K. Leo, Appl. Phys. Lett. **89**, 083509 (2006).
[11] H. Bässler, Phys. Status Solidi B **175**, 15 (1993).
[12] M. v. d. Auweraer, F. C. d. Schryver, P. M. Borsenberger, and H. Bässler, Adv. Mater. **6**, 199 (1994).
[13] H. Bässler and H. Killesreiter, Phys. Status Solidi B **53**, 183 (1972).
[14] X. Feng, V. Marcon, W. Pisula, M. R. Hansen, J. Kirkpatrick, F. Grozema, D. Andrienko, K. Kremer, and K. Müllen, Nat. Mater.**8**, 421 (2009).
[15] T. Vehoff, Y. S. Chung, K. Johnston, A. Troisi, D. Y. Yoon, and D. Andrienko, J. Phys. Chem. C**114**, 10592 (2010).
[16] W. F. Pasveer, J. Cottaar, C. Tanase, R. Coehoorn, P. A. Bobbert, P. W. M. Blom, D. M. de Leeuw, and M. A. J. Michels, Phys. Rev. Lett. **94**, 206601 (2005).
[17] S. L. M. van Mensfoort, S. I. E. Vulto, R. A. J. Janssen, and R. Coehoorn, Phys. Rev. B **78**, 085208 (2008).
[18] M. Bouhassoune, S. L. M. van Mensfoort, P. A. Bobbert, and R. Coehoorn, Org. Electron. **10**, 437 (2009).
[19] R. Coehoorn and S. L. M. van Mensfoort, Phys. Rev. B **80**, 085302 (2009).
[20] M. Schober, S. Olthof, M. Furno, B. Lüssem, and K. Leo, Appl. Phys. Lett. **97**, 013303 (2010).
[21] A. Miller and E. Abrahams, Phys. Rev. **120**, 745 (1960).
[22] R. J. de Vries, S. L. M. van Mensfoort, V. Shabro, S. I. E. Vulto, R. A. J. Janssen, and R. Coehoorn, Appl. Phys. Lett. **94**, 163307 (2009).
[23] D. L. Scharfetter and H. K. Gummel, IEEE Trans. Electron Devices **16**, 64 (1969).
[24] J. Staudigel, M. Stößel, F. Steuber, and J. Simmerer, J. Appl. Phys. **86**, 3895 (1999).
[25] V. I. Arkhipov, P. Heremans, E. V. Emelianova, G. J. Adriaenssens, and H. Bässler, Appl. Phys. Lett. **82**, 3245 (2003).
[26] S. Mladenovski, S. Reineke, and K. Neyts, Opt. Lett. **34**, 1375 (2009).
[27] R. Meerheim, M. Furno, S. Hofmann, B. Lüssem, and K. Leo, Appl. Phys. Lett. **97**, 253305 (2010).
[28] P. Freitag, S. Reineke, S. Olthof, M. Furno, B. Lüssem, and K. Leo, Org. Electron. **11**, 1676 (2010).
[29] S. Olthof, R. Meerheim, M. Schober, and K. Leo, Phys. Rev. B **79**, 245308 (2009).